High-Performance Nonfullerene Organic Photovoltaics Applicable for Both Outdoor and Indoor Environments through Directional Photon Energy Transfer

Yong Woon Han, Chang Ho Jung, Hyoung Seok Lee, Sung Jae Jeon, and Doo Kyung Moon*

Read Online

ACCESS | Metrics & More | Article Recommendations | Supporting Information

ABSTRACT: With the advent of the smart factory and the Internet of Things (IoT) sensors, organic photovoltaics (OPVs) gained attention because of their ability to provide indoor power generation as an off-grid power supply. To satisfy these applications, OPVs must be capable of power generation in both outdoor and indoor at the same time for developing environmentally independent devices. For high performances in indoor irradiation, a strategy that maximizes photon utilization is essential. In this study, graphene quantum dots (GQDs), which have unique emitting properties, are introduced into a ZnO layer for efficient photon utilization of nonfullerene-based OPVs under indoor irradiation. GQDs exhibit high absorption properties in the 350−550 nm region and strong emission properties in the visible region due to down-conversion from lattice vibration. Using these properties, GQDs provide directional photon energy transfer to the bulk-heterojunction (BHJ) layer because the optical properties overlap. Additionally, the GQD-doped ZnO layer enhances shunt resistance (R_{Sh}) and forms good interfacial contact with the BHJ layer that results in increased carrier dissociation and transportation. Consequently, the fabricated device based on P(Cl-Cl)(BDD = 0.2) and IT-4F introduces GQDs exhibiting a maximum power conversion efficiency (PCE) of 14.0% with a superior enhanced short circuit current density (J_{SC}) and fill factor (FF). Furthermore, the fabricated device exhibited high PCEs of 19.6 and 17.2% under 1000 and 200 lux indoor irradiation of light emitting diode (LED) lamps, respectively.

KEYWORDS: indoor solar cells, organic solar cells, graphene quantum dots, large area device, photon energy transfer
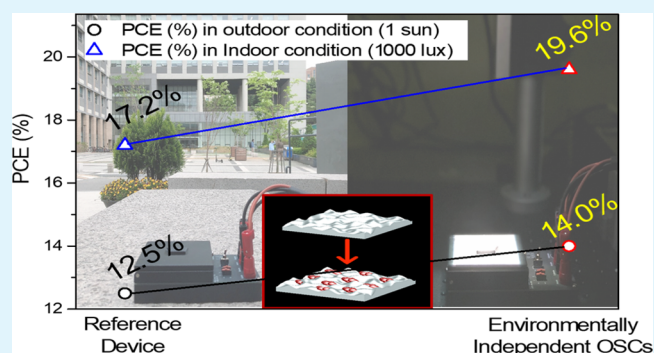
1. INTRODUCTION

Organic photovoltaics (OPVs) are efficient in manufacturing large-area, flexible, and semi-transparent devices using organic semiconductors, which have been applied in various fields including off-grid power supply, building-integrated photovoltaics (BIPVs), and Internet of Things (IoT) sensors.[1−4] Recent research strategies for the application of OPVs, such as the design of photoactive materials, introduction of buffer layers, and modification of device structure, have been reported to achieve a high PCE of not less than 17%.[5−7] Furthermore, as flexible large-area modules are manufactured through an all-solution process, the results of these studies have been essential for realizing the commercialization of OPVs.[8]

Conventionally, solar cells are used in outdoor environments with the aim of absorbing and utilizing broad solar irradiation (AM 1.5G); however, recent off-grid applications have problems of requiring high power generation for indoor irradiation (200−1000 lux), such as a smart factory, living room, and an office.[9] Although commercialized crystalline silicon (c-Si) solar cells exhibit a high performance in solar irradiation, they exhibit a sharp drop in the performance due to the variation of incident light angle and illumination intensity, which is inapplicable to indoor power supply.[10,11] Thus, there is an increasing demand for OPVs that can effectively utilize the emission properties (high emission intensity: $\lambda = 450−600$ nm) of LED lamps used as indoor lightings.[10,12]

The generation of many effective carriers should be induced by increasing the optical properties of the OPVs to improve their performance in outdoor irradiation. Devices known as ternary OPVs, whose photoactive layer introduces a third component, are considered to be a good strategy because the enhanced optical properties and increased carrier transport of the devices can effectively achieve high performances.[13,14]
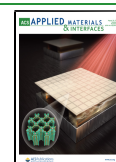
Meanwhile, in indoor irradiation, OPVs exhibit a low short circuit current density (J_{SC}) due to absolutely insufficient light intensity, as well as a low open circuit voltage (V_{OC}) due to energetic mismatch resulting from energy loss, which requires a complementary strategy.[15,16] Gao, Hou, and co-workers developed a small-molecule acceptor, IO-4Cl, to minimize energy loss, and simultaneously achieved a PCE of up to 26.1% as well as a V_{OC} of 1.10 V through spectral matching, under 1000 lux of a 2700 K LED lamp (high emission intensity at λ = 500−700 nm).[9] Additionally, inverted-structured OPVs are being studied in various perspectives because of optoelectronic advantages of introducing a ZnO layer for improving performances both in ambient and indoor environments.[17−20] As the ZnO can act as an optical spacer for higher photon utilization due to its unique optical properties,[21,22] the incident light can be amplified effectively under indoor lighting.[18−20] In addition, because the pristine ZnO layer usually exhibits a "light-soaking" issue, so, a "doping strategy" is needed for enhancing photon utilization.[23,24] Also, general ZnO layers suffered from lower air stability and degradation resulted from surface defects; so, the surface-modified strategy is needed to solve the problems.[25,26] Accordingly, an efficient photon utilization technique should be developed for high performances of OPVs in outdoor and indoor irradiation.

As a strategy for efficient utilization of photons in OPVs, quantum dots (QDs) that have high emission and unique optical properties can be introduced. Many previous studies involving our results succeeded in significantly enhancing optical properties through Förster resonance energy transfer effects by introducing QDs into a polymer-based BHJ layer.[27−29] Among QDs, graphene QDs (GQDs) have been used for diverse applications, including catalysts and transparent electrodes, because GQDs can exhibit excellent optoelectronic properties through controlling the size and the functional groups.[30−34] Park, Hong, and co-workers introduced graphene oxide QDs and GQDs into a poly[[4,8-bis[(2-ethylhexyl)oxy]benzo[1,2-b:4,5-b′]dithiophene-2,6-diyl][3-fluoro-2-[(2-ethylhexyl)carbonyl]thieno[3,4-b]-thiophenediyl]] (PTB7) and [6,6]-phenyl-C71-butyric acid methyl ester (PC$_{71}$BM)−based BHJ layer to achieve a PCE of up to 7.6% through enhanced absorptivity and conductivity.[32] Lee, Bae, and co-workers introduced nitrogen self-doped GQDs into poly(3,4-ethylenedioxythiophene)-poly(styrene sulfonate) (PEDOT:PSS), which was a hole transport layer (HTL), to achieve a PCE of up to 8.5% through energy level shift and high conductivity.[33] Furthermore, diverse studies have been conducted on methods of utilizing the advantages of optoelectronic properties, such as introducing fast exciton dissociation effects of functionalized GQDs to improve the performance of OPVs.[34]

In this study, we introduced GQDs that have unique emitting properties into a ZnO layer as an additional emissive dopant. GQDs are representative emissive QDs, exhibiting absorption properties in the λ = 350−550 nm region, as well as strong emission properties in the visible range.[31,33] In addition, we introduced P(Cl-Cl)(BDD = 0.2) terpolymer as a high potential candidate for outdoor and indoor environments. The P(Cl-Cl)(BDD = 0.2) terpolymer exhibits a balance between molecular weight and solubility, enabling application of eco-friendly nonhalogenated solvents.[35]

In particular, we focused on the overlap between the unique emission region of GQDs and the absorption region of an organic photoactive layer. The combination of P(Cl-Cl)(BDD = 0.2), which was a high-performance donor, and 3,9-bis(2-methylene-((3-(1,1-dicyanomethylene)-6,7-difluoro)-indanone))-5,5,11,11-tetrakis(4-hexylphenyl)-dithieno[2,3-d:2′,3′-d′]-s-indaceno[1,2-b:5,6-b′]dithiophene (IT-4F) as an acceptor enabled photon energy transfer to the nonfullerene acceptor (NFA)-based BHJ layer. The directional photon energy transfer from GQDs to P(Cl-Cl)(BDD = 0.2) occurred due to optical overlap, thereby enhancing the optical properties of the BHJ layer. Consequently, the introduction of the GQD-doped ZnO layer resulted in high-performance PCEs of 14.0% (under 1 sun), 17.6%, and 19.6% (under 200 and 1000 lux) in outdoor irradiation (AM 1.5G, xenon lamp) as well as indoor irradiation (200 and 1000 lux of 5000 K white LED lamp), respectively. These results were obtained by the efficient photon utilization owing to a superior quantum efficiency of over 80% and high shunt resistance (R_{Sh}).

2. EXPERIMENTAL SECTION

2.1. Materials for Fabrication of OPVs. P(Cl-Cl)(BDD = 0.2) used as a donor was synthesized following previous literature.[35] IT-4F used as an acceptor was purchased from 1-Materials (Canada). Xylene (o-XY) and 1-phenylnaphthalene (PN) used as a solvent and additives were purchased from Sigma-Aldrich (Germany). Zinc acetate dihydrate [Zn(CH$_3$COO)$_2$·2H$_2$O], ethanolamine, and 2-methoxyethanol used as precursors of sol−gel ZnO were purchased from Sigma-Aldrich (Germany). Graphene quantum dots (GQDs, average size of QDs was around 5 nm) used as an emissive dopant of ZnO was purchased from Sigma-Aldrich (Germany).

2.2. Fabrication of OPVs. For fabrication of OPVs, a cleaning process was performed for patterned ITO glasses through ultra-sonication in the order of neutral detergent, isopropyl alcohol, and deionized water. UV-ozone (UVO) treatment in a UVO cleaner (Ahtech LTS) was performed for the cleaned glasses. The OPVs were fabricated into inverted structure (ITO/ZnO/photoactive layer/MoO$_3$/Ag) with optimized conditions and processes. The ZnO layer formed through a sol−gel method. Zinc acetate dihydrate and ethanolamine (1:1 molar ratio) were dissolved to 2-methoxyethanol (0.75 M); then, the solution was stirred for 12 h with a temperature of 60 °C. The final ZnO precursor obtained a clear solution.[36] The prepared ZnO precursor was coated onto cleaned ITO glasses at 3000 rpm then annealed at 150 °C for 30 min. For introducing an emissive dopant, GQDs were distributed to the ZnO precursor with a concentration of 1−2 mg mL^{-1}. The photoactive layer consisted of P(Cl-Cl)(BDD = 0.2)/IT-4F formed with a ratio of 1:1 (20 mg mL^{-1}). After coating of the photoactive layer, the films were annealed at 140 °C for 10 min. Finally, the hole transport layer (HTL) and top electrode were formed through a thermal evaporation process in a vacuum chamber (under 10^{-7} Torr) with the thicknesses of 5 and 100 nm, respectively. The active areas of the general device and large-area device were 0.04 and 1.0 cm^2, respectively.

2.3. Characterization of the Fabricated Devices. The emission properties of pristine ZnO and GQD-doped ZnO solution were characterized with a UV hand lamp (emitted at 365 nm, VL-4L). The absorption and emission properties of pristine ZnO and GQD-doped ZnO films were measured through a UV−vis spectrometer (Agilent 8453) and a photoluminescence spectrometer (LS55, PerkinElmer), respectively. The current density−voltage ($J−V$) and dark $J−V$ characteristics were measured using a power source meter (Keithley 2400) and a solar simulator (Oriel, AM 1.5G under an illumination of 100 mW cm^{-2} with a Xe lamp). The external quantum efficiency (EQE), internal quantum efficiency (IQE), and calculated current density characteristics were measured with an incident photon-to-current efficiency (IPCE) measurement system (Polaronix K3100, Mc Science). The indoor performances of fabricated OPVs were measured with an LED lamp indoor solar simulator (Indoor light simulator YILS series, AAA class, Yamashita Denso) under irradiation of 200 and 1000 lux. The energy level alignment was measured using ultraviolet photoelectron spectroscopy analysis
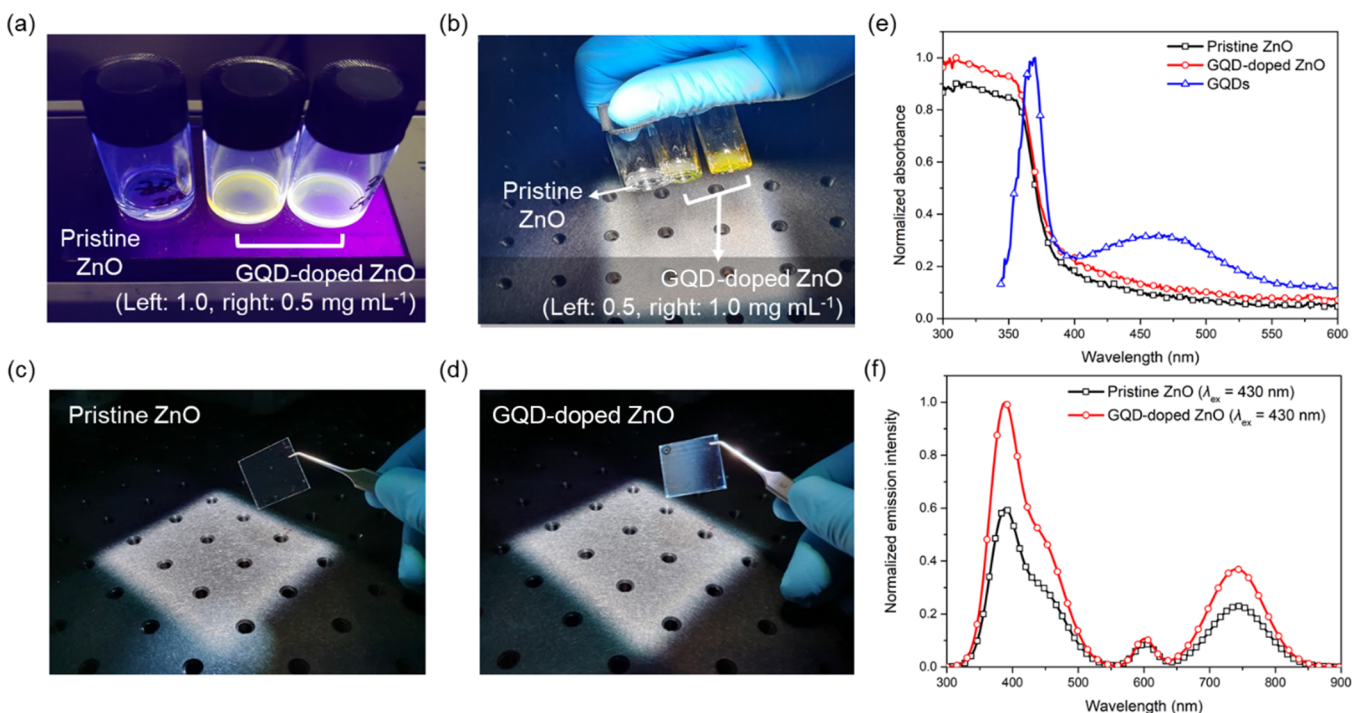
Figure 1. Images of pristine ZnO and GQD-doped ZnO solutions (a) under a UV lamp (emission at 365 nm) and (b) under an indoor LED lamp (emission at 400−780 nm). Images of manufactured films introduced with (c) pristine ZnO layer and (d) GQD-doped ZnO layer under an LED lamp. (e) Absorption properties and (f) emission properties of the pristine ZnO film and GQD-doped ZnO film (the absorption property of GQDs is shown in e).

(AXIS-NOVA, Kratos). The optical energy level was calculated from a UV−vis spectrometer using a Tauc plot. The optical simulation characteristics were performed using finite-difference time-domain (FDTD) solution software (Ansys, Inc.). The contact angle and surface energy characteristics were measured using a contact angle analyzer (DSA100, KRUSS). The surface morphology and surface potential characteristics were measured using field emission scanning electron microscopy (FE-SEM; SU8010, Hitachi), atomic force microscopy (AFM), and electrostatic force microscopy (EFM) (PSIA XE-100, Park Systems). The crystalline structures were measured using grazing incidence wide-angle X-ray scattering (GIWAXS) at the 3C beamline in Pohang Accelerator Laboratory (PAL), Republic of Korea. The time-resolved photoluminescence (TRPL) decay measurement was performed using a confocal microscope (MicroTime-200, Picoquant, Germany). The lifetime measurements were performed at the Korea Basic Science Institute (KBSI), Daegu Center, Republic of Korea.

3. RESULTS AND DISCUSSION

3.1. Optical Properties of the GQD-Doped ZnO Layer.
This study introduced GQDs to a ZnO precursor solution that was used as ETLs for OPVs to utilize excellent optical benefits of GQDs. Under an ultraviolet (UV) lamp (λ = 365 nm) and a light emitting diode (LED) lamp (main emission at λ = 400− 780 nm), a pristine ZnO solution exhibited extremely weak emission properties, while a GQD-doped ZnO solution exhibited strong emission properties (Figure 1a,b). In particular, under an indoor LED lamp, the GQD-doped ZnO solution exhibited strong yellowish emission properties. After forming films, the pristine ZnO film under the LED lamp exhibited insignificant change (Figure 1c), as in the solution state; however, the GQD-doped ZnO film exhibited strong yellowish emission properties, which were noticeable (Figure 1d).

Figure 1e shows the absorption and emission properties of ETLs formed in this study. The pristine ZnO layer exhibited absorption properties in the region of λ = ∼400 nm. The GQDs exhibited a maximum absorption peak in the region of λ = 350−400 nm, as well as absorption properties in the region of λ = ∼550 nm.[31,33] Accordingly, the GQD-doped ZnO layer exhibited relatively enhanced absorption properties in the entire region compared to the pristine ZnO layer. These results, as observed in photoluminescence (PL) measurement, were obtained because of the unique emission properties of GQDs. The GQD-doped ZnO film, which was excited at λ = 430 nm, exhibited higher emission properties compared with the pristine ZnO film (in Figure 1f). This is because GQDs are capable of down-conversion through lattice vibration, and they exhibit strong redshifted emission properties through a higher degree of surface oxidation.[30,37] Furthermore, the GQD-doped ZnO exhibited fewer surface defects with relatively low emission properties in the range of λ = 550−650 nm.[38,39]

3.2. Photovoltaic Properties under 1 Sun and Indoor Irradiation.
These results reflect that strong and unique emission properties of GQDs can contribute toward enhancing the performance of OPVs as an additional emissive dopant. Based on P(Cl-Cl)(BDD = 0.2) and IT-4F, which were a high-performance nonfullerene acceptor (NFA) system, Figure 2 and Table 1 show characterization results of the inverted-structured devices (ITO/electron transport layer (ETL)/active layer/MoO₃/Ag, active area of 0.04 cm²) under 1 sun and indoor irradiation that were manufactured by the introduction of the GQD-doped ZnO layer. The P(Cl-Cl)(BDD = 0.2) exhibits a high performance through an eco-friendly process in combination with the IT-4F through a balanced molecular weight and crystallinity characteristics (Figure 2a,b).[35] Additionally, P(Cl-Cl)(BDD = 0.2) and IT-4F show absorption
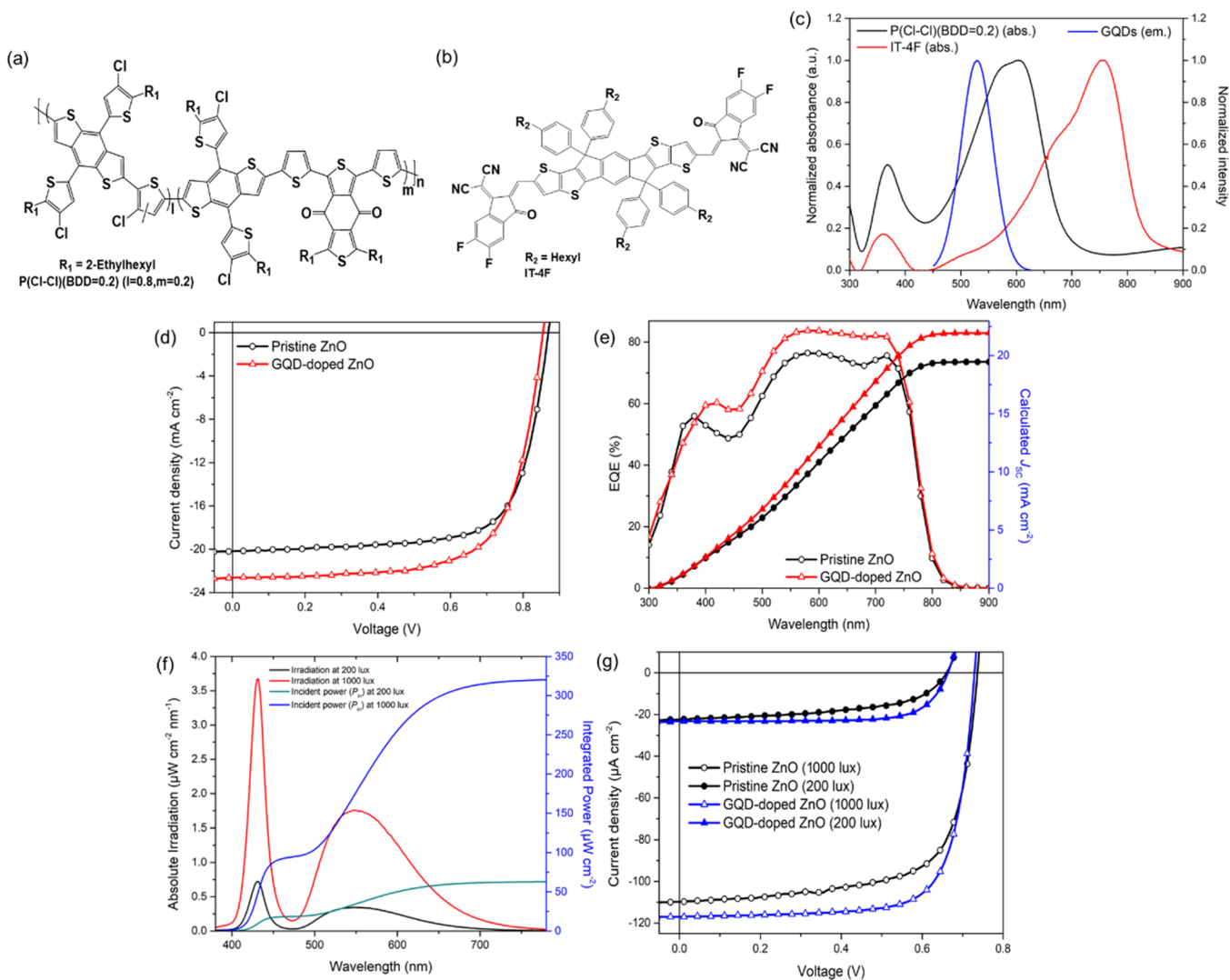
Figure 2. Chemical structures of (a) P(Cl-Cl)(BDD = 0.2) and (b) IT-4F introduced as photoactive materials. (c) Absorption properties of P(Cl-Cl)(BDD = 0.2) and IT-4F and emission properties of GQDs. (d) Current density−voltage (J−V) characteristics and (e) external quantum efficiency (EQE) characteristics of fabricated inverted-structured devices (ITO/ETLs/BHJ layer/MoO$_3$/Ag active area of 0.04 cm^2) (open symbols indicate EQE; closed symbols indicate calculated J_{SC}). (f) Absolute irradiation and integrated power properties of a 5000 K LED lamp at 1000 and 200 lux measured using a photo-radiometer (HD2102) and calculated from software. (g) Indoor J−V characteristics under 1000 and 200 lux irradiation of an LED lamp (5000 K).

Table 1. Photovoltaic Performances of Fabricated OSCs under 1 Sun Irradiation[a]

ETLs	J_{SC} [mA cm^{-2}]	V_{OC} [V]	FF [%]	PCE$_{max}$[b] [%]	R_{Sh} [Ω cm^2]	R_S [Ω cm^2]
pristine ZnO	20.2 (20.0 ± 0.21)	0.878 (0.869 ± 0.01)	70.5 (70.1 ± 0.43)	12.5	874	4.0
GQD-doped ZnO[c]	22.6 (22.5 ± 0.11)	0.858 (0.848 ± 0.01)	72.1 (71.8 ± 0.33)	14.0	2127	3.1

[a]Devices were fabricated with inverted structure (ITO/ETLs/BHJ layer/MoO$_3$/Ag, active area = 0.04 cm^2). [b]The maximum value was obtained from the best performance among 10 fabricated devices. [c]The concentration of graphene QDs into the ZnO layer is 1.0 mg mL^{-1}.

properties around λ = 450−700 nm and λ = 500−850 nm, respectively, and GQDs exhibit emission properties around λ = 450−630 nm (shown in Figure 2c). With these optical properties, the emission range of GQDs and the absorption range of P(Cl-Cl)(BDD = 0.2) are largely overlapped being expected that energy transfer will occur.

In particular, the device with the pristine ZnO layer as an ETL exhibited a PCE of up to 12.5% (J_{SC} = 20.2 mA cm^{-2}, V_{OC} = 0.878 V, and FF = 70.5%). Additionally, the devices that were manufactured by introducing the GQD-doped ZnO layer exhibited a PCE of up to 14.0% (J_{SC} = 22.6 mA cm^{-2}, V_{OC} =

0.858 V, and FF = 72.1%), as a result of a significantly improved J_{SC} and FF (Figure 2d). Furthermore, there was a significant difference in the J_{SC} depending on the doping concentration in the GQDs (Figure S1 and Table S1). The devices exhibited relatively high J_{SC} and FF values at low concentrations of the GQDs, further exhibiting the highest J_{SC} corresponding to the maximum PCE at an optimized concentration. However, the devices exhibited low FF at high concentrations of the GQDs.

These results are consistent with the external quantum efficiency (EQE) characteristics shown in Figure 2e. The

Table 2. Photovoltaic Performances of Fabricated OSCs under Different Light Intensities with an LED Lamp (5000 K)[a]

ETLs	light source [lux]	P_{in} [$\mu W\ cm^{-2}$]	J_{SC} [$\mu A\ cm^{-2}$]	V_{OC} [V]	FF [%]	$P_{out,max}$ [$\mu W\ cm^{-2}$]	PCE_{max}[b] [%]
pristine ZnO	200	62.8	21.9 (21.5 ± 0.37)	0.663 (0.643 ± 0.02)	54.2 (53.9 ± 0.29)	7.3	12.5
	1000	320.2	109.2 (108.7 ± 0.52)	0.737 (0.717 ± 0.02)	68.5 (68.0 ± 0.49)	51.8	17.2
GQD-doped ZnO	200	62.8	23.3 (23.0 ± 0.29)	0.660 (0.640 ± 0.02)	71.9 (71.6 ± 0.31)	10.4	17.6
	1000	320.2	116.7 (116.4 ± 0.31)	0.728 (0.708 ± 0.02)	73.7 (73.4 ± 0.28)	58.9	19.6

[a]Devices were fabricated with inverted structure (ITO/ETLs/BHJ layer/MoO$_3$/Ag, active area = 0.04 cm^2). [b]The maximum value was obtained from the best performance among 10 fabricated devices.
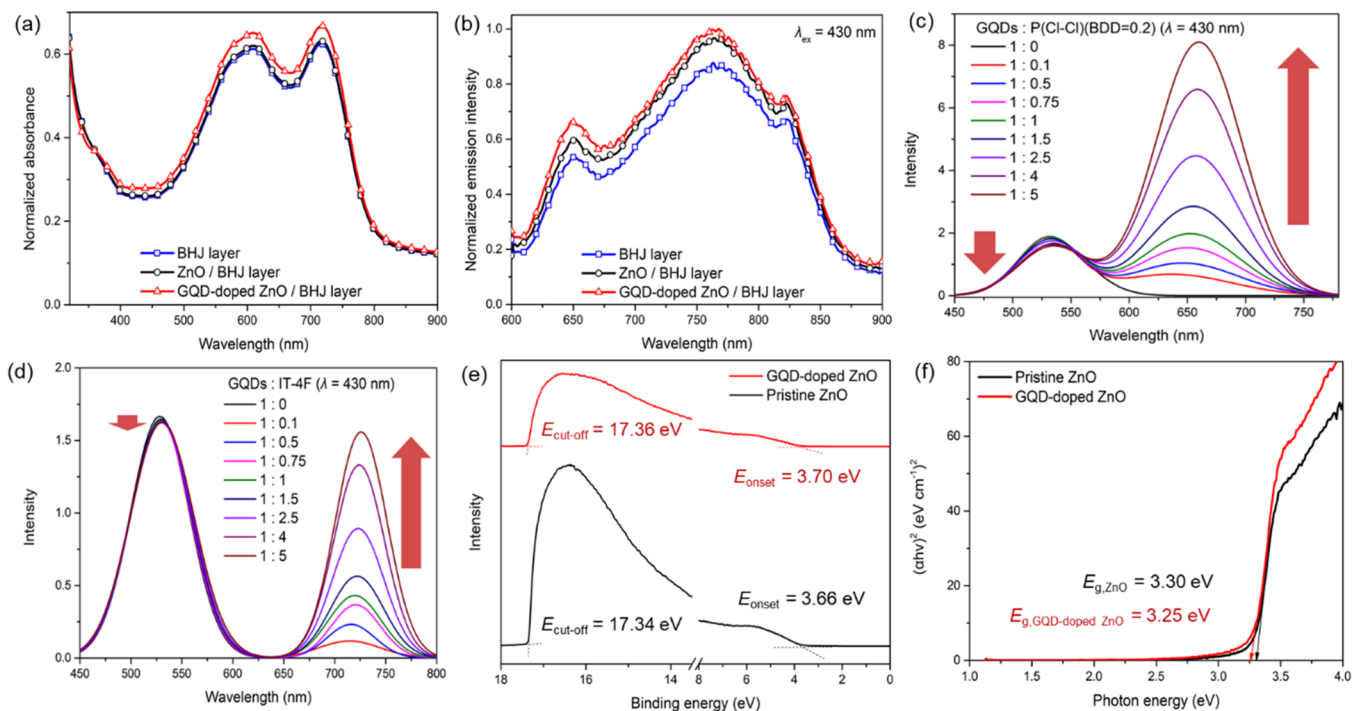

Figure 3. (a) Absorption characteristics of the pristine BHJ layer and BHJ layers coated onto ETLs and (b) emission characteristics of the pristine BHJ layer and BHJ layers coated onto ETLs against an excitation wavelength of GQDs at 430 nm. Emission tendency spectra of GQDs with doping of (c) P(Cl-Cl)(BDD = 0.2) and (d) IT-4F at an excitation wavelength of GQDs at 430 nm. (e) UPS characteristics and (f) Tauc plot against photon energy characteristics of the pristine ZnO layer and GQD-doped ZnO layer.

calculated J_{SC} (cal. J_{SC}) values of the pristine ZnO and GQD-doped ZnO from the EQE characteristics were 19.44 and 21.92 mA cm^{-2}, respectively. Additionally, the cal. J_{SC} values with respect to doping concentration of the GQDs were 19.79, 21.92, and 20.89 mA cm^{-2}, respectively (in Figure S1b). The introduction of the GQDs reduced the intensity of the short-wavelength region under λ = 400 nm and significantly increased the intensity in the λ = 400−800 nm region. This is because the introduction of the GQDs provided optical benefits to the BHJ layer.

Furthermore, to utilize the optical benefits of the GQDs, the fabricated devices were characterized under a white LED lamp for diverse indoor irradiation (5000 K lamp, under 1000 and 200 lux conditions). The absolute irradiation and integrated power properties of LED lamp are shown in Figure 2f, and photovoltaic properties under indoor irradiation are shown in Figure 2g and Table 2. For typical indoor usage, measurements were obtained in an irradiation environment of an LED lamp similar to the illuminance commonly used in offices and living rooms. The devices with the pristine ZnO layer exhibited PCEs of 12.5 and 17.2% (the maximum output powers were 7.3 and 51.8 μW cm^{-2}) at 200 and 1000 lux, respectively. Additionally, the devices with the GQD-doped ZnO layer exhibited PCEs of

17.2 and 19.6% (the maximum output powers were 10.4 and 58.9 μW cm^{-2}), and particularly, the introduction of the GQDs significantly improved J_{SC} and FF. Generally, the population of photogenerated carriers and interaction among carriers decreased at low light intensities, exhibiting low performances due to high trap-assisted recombination.[16,40] However, the introduction of the GQDs enabled efficient utilization of absorbed light even in low incident irradiation through additional emissive properties. Accordingly, the devices fabricated with the GQD-doped ZnO layer exhibited high performances in 1 sun and indoor irradiation.

3.3. Optoelectronic Properties. In the BHJ layer with the GQD-doped ZnO layer (GQD-doped ZnO/BHJ layer), it exhibited relatively higher absorption properties compared with the pristine one (BHJ layer) or with the pristine ZnO layer (ZnO/BHJ layer) (Figure 3a). In particular, the introduction of GQDs improved absorption properties at λ = 350−800 nm. Also, the emission properties of the pristine BHJ layer and the BHJ layers with the pristine ZnO layer or GQD-doped ZnO layer were measured (shown in Figure 3b). The measurement results at λ = 430 nm indicated that the emission intensity of ZnO/BHJ and GQD-doped ZnO/BHJ layers increased by 11.36 and 16.58% compared with the pristine
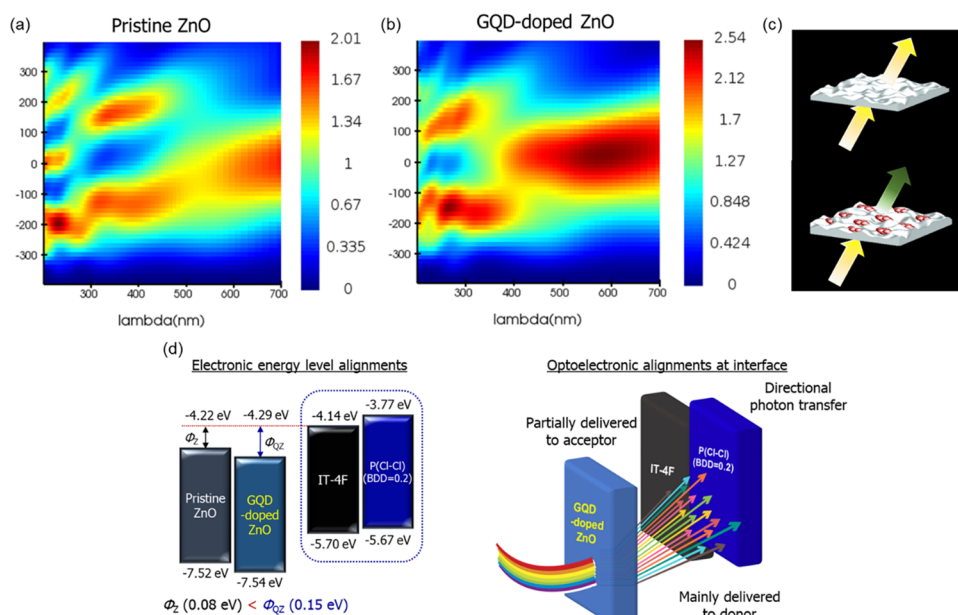
Figure 4. Optical simulation characteristic results of (a) pristine ZnO layer and (b) GQD-doped ZnO layer with the electric field distributions (|E|) of incident light calculated by FDTD solution (red: optically high response region, blue: low response region). (c) Simulated models (top: pristine ZnO layer, bottom: GQD-doped ZnO layer). (d) Derived illustration of electronic energy level alignments and optoelectronic alignments between ZnO layers and the BHJ layer consisted of a donor and acceptor (left: electronic energy level alignments explaining electron barriers (Φ_Z, Φ_{QZ}), right: optoelectronic alignments explaining directional photon transfer to the donor).

BHJ layer (Table S2). Additionally, we measured emission properties of GQDs with doping of photoactive materials at an excitation wavelength of GQDs (at λ = 430 nm) (shown in Figure 3c,d). The pristine GQDs exhibited emission spectra around λ = 450−600 nm (black line of Figure 3c). When the P(Cl-Cl)(BDD = 0.2) doped to GQDs, an emission peak of GQDs (at λ = 450−600 nm) decreased, and an emission peak of P(Cl-Cl)(BDD = 0.2) (at λ = 600−750 nm) largely increased (a maximum increase ratio of 5.08) (shown in Figure 3c). However, when the IT-4F doped to GQDs, an emission peak of IT-4F (at λ = 650−800 nm) increased, but these increases were lower than the emission peak of pristine GQDs (shown in Figure 3d). These results indicate that direct energy transfer from GQDs to P(Cl-Cl)(BDD = 0.2) occurred mainly and relatively low energy transfer to IT-4F.[41]

The emission properties of GQDs with doping of photo-active materials and emission properties of BHJ layers (at λ = 530, 630 nm) are shown in Figure S2. At an excitation wavelength of P(Cl-Cl)(BDD = 0.2) (λ = 530 nm), the maximum increase ratio was large with approximately 8.0 (Figure S2a). However, when the IT-4F doped to GQDs, at an excitation wavelength of IT-4F (λ = 630 nm), the maximum increase ratio was lower than P(Cl-Cl)(BDD = 0.2) with approximately 4.0 (Figure S2b). On the other hand, with respect to BHJ layers, the emission properties of the BHJ layer formed onto the GQD-doped ZnO layer exhibited higher intensity than those of pristine one at both λ = 530 and 630 nm (Figure S2c,d and Table S2). Consequently, these results indicate that the GQD-doped ZnO layer exhibits significant enhancement of optoelectronic properties due to energy transfer to P(Cl-Cl)(BDD = 0.2) with optical overlap. In particular, because there was a strong energy transfer from the GQD-doped ZnO layer to the BHJ layer, effective carriers increased, showing high emission intensity.[27,42,43] Consequently, the introduction of GQDs induced strong emission

properties, enhanced the optical properties of the BHJ layer, and increased effective photogenerated carriers.

In this study, we also performed ultraviolet photoelectron spectroscopy (UPS) to analyze the increased effective photogenerated carriers in terms of carrier transport and energy transfer due to the introduction of the GQD-doped ZnO layer (in Figure 3e). Energy cutoff (E_{cutoff}) and onset (E_{onset}) values were obtained from the UPS measurement; thereby, the valence band energy levels (E_{VB}) of the pristine ZnO and GQD-doped ZnO were calculated using the equation below.[44,45]

$$E_{VB} = h\nu - (E_{cutoff} + E_{onset}) \qquad (1)$$

The calculated results are as follows. For the pristine ZnO layer, the E_{cutoff} = 17.34 eV and the E_{onset} = 3.66 eV, and for the GQD-doped ZnO layer, $E_{cut-off}$ = 17.36 eV and E_{onset} = 3.70 eV. Furthermore, for the optical band gap energy properties that were calculated the through absorption properties (Figure 1e) and Tauc plot, the pristine ZnO = 3.30 eV and the GQD-doped ZnO = 3.25 eV, respectively (in Figure 3f).[46]

The electric field distributions were calculated by finite-difference time domain (FDTD) analysis for investigating optical response of the GQD-doped ZnO layer (shown in Figure 4a,b). The light similar with solar lay was transmitted to pristine ZnO and GQD-doped ZnO layers. The electric field distributions of passed light through the GQD-doped ZnO layer exhibited higher optical response in λ = 400−700 nm due to strong emission properties of GQDs. Then, the simulated models are shown in Figure 4c. The GQD-doped ZnO layer contributed to more emission in the visible range after absorbing light, indicating availability for strong energy transfer to the BHJ layer.

With these results, we estimated electronic energy level alignments and optoelectronic alignments at interfaces between the ETL and BHJ layer, and the results are shown
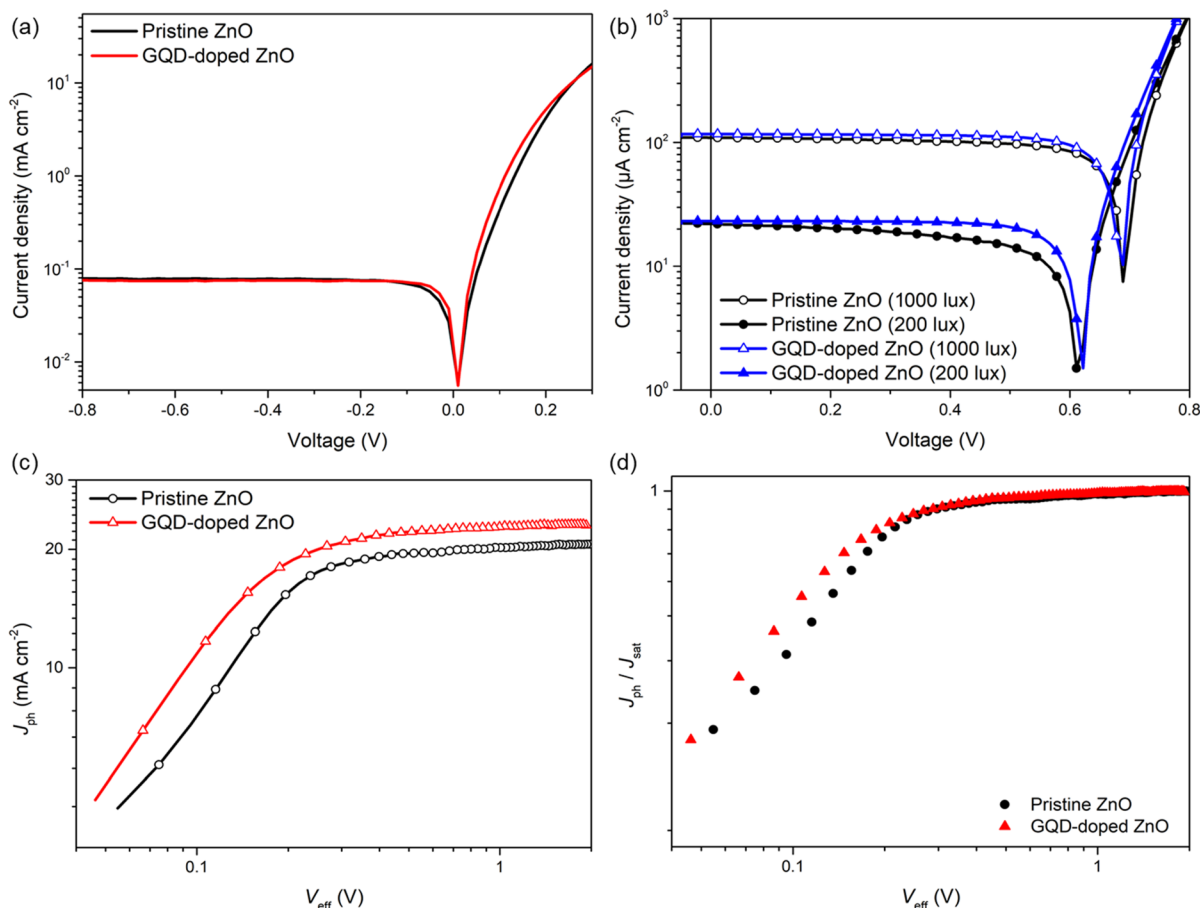
Figure 5. Semi-log plot of (a) dark $J-V$ under 1 sun irradiation and (b) indoor $J-V$ characteristics under 1000 and 200 lux of a white LED lamp (5000 K). (c) Photocurrent density–effective voltage ($J_{ph}-V_{eff}$) characteristics and (d) carrier dissociation probability of fabricated devices.

in Figure 4d. the conduction band energy levels (E_{CB}) of the pristine ZnO and the GQD-doped ZnO layers were derived based on the calculated E_{VB} and optical band gap energy (in Figure 4d). For the pristine ZnO layer, the E_{CB} = −4.22 eV, and E_{VB} = −7.52 eV, showing the electron barrier (Φ_Z) characteristics of approximately 0.08 eV with the lowest unoccupied molecular orbital (LUMO) level of IT-4F (−4.14 eV). However, for the GQD-doped ZnO layer, the E_{CB} = −4.29 eV, and E_{VB} = −7.54 eV, showing the electron barrier (Φ_{QZ}) characteristics of approximately 0.15 eV. These results are due to energy level shift by the work function of GQDs (−4.2 to −4.5 eV).[47]

In addition, surface potential properties of films were measured via electrostatic force microscopy (EFM) analysis (shown in Figure S3). The pristine ZnO film and GQD-doped ZnO film exhibited surface potentials of 524.538 and 512.206 mV, respectively. These results suggest that the lower surface potential with an electronic stable status of the GQD-doped ZnO layer exhibit a higher work function than the pristine ZnO layer.[48] Accordingly, an energy level mismatch occurred, resulting in a slightly low V_{OC} of 0.858 V because the introduction of the GQD-doped ZnO layer rather than the pristine ZnO layer formed relatively large energy barriers. In other words, the enhanced emission intensity occurred mainly owing to energy transfer by introducing the GQD-doped ZnO layer.

As shown in Figure 4d, the enhancement in emission properties of the GQD-doped ZnO layer induced energy

transfer to the BHJ layer. In particular, owing to the emission properties increased in the region of λ = 500−800 nm, high photon energy transfer and partial photon energy transfer occurred to the P(Cl-Cl)(BDD = 0.2) and IT-4F, respectively. These results are because the emission properties of the GQD-doped ZnO layer and the absorption properties of the P(Cl-Cl)(BDD = 0.2) exhibited large spectral overlap.[27,43,49] Therefore, the GQD-doped ZnO layer contributed to the enhancement in optical properties and effective photogenerated carriers of the BHJ layer through directional photon transfer to the P(Cl-Cl)(BDD = 0.2) as well as partial photon transfer to the IT-4F. These results imply that the GQDs can help in photon transfer to the BHJ layer, and then, it enabled efficient photon utilization.

3.4. Fill Factor (FF) and Shunt Resistance Theory. Devices with the GQD-doped ZnO layer exhibited higher internal quantum efficiency (IQE) properties compared with pristine devices, showing efficient photon utilization (Figure S4).[50] Additionally, as shown in Figure S5, the FF initially increased (FF of 75% in a device with the GQD-doped ZnO layer) and thereafter decreased along with a decrease in light intensity. Generally, the FF is a function of shunt resistance (R_{Sh}) and carrier recombination, which is a key factor in determining OPVs' performance in the Shockley−Queisser model.[51,52] In particular, in the equivalent circuit model of OPVs, FF and ideal FF (FF_0) can be represented by the equations below.

$$FF_0 = v_{oc} - \ln(v_{oc} + 0.72)/(v_{oc} + 1) \tag{2}$$
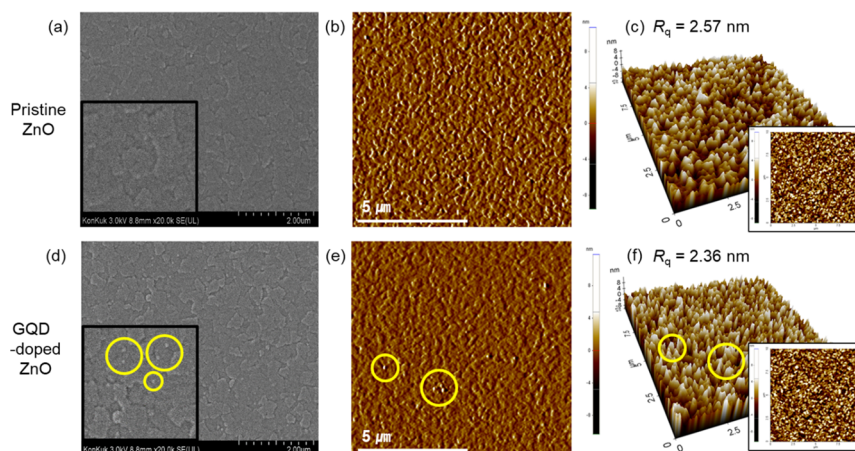
Figure 6. Surface phase and morphology characteristics measured via FE-SEM and AFM of (a−c) pristine ZnO layer and (d−f) GQD-doped ZnO layer (the insets of a and d are the partial enlarged images, and the insets of c and f are the 2D images of morphology).

$$FF_S = FF_0(1 - \gamma_s) \tag{3}$$

Here, v_{oc}, FF_S, and γ_s refer to the normalized V_{OC} ($v_{oc} = eV_{OC}/nkT$, where e, n, k, and T are the elementary charge, diode ideality factor, Boltzmann constant, and absolute temperature), series fill factor, and normalized series resistance (R_S/R_{ch}, where R_{ch} is the characteristic resistance related to $R_{ch} = V_{OC}/A{\times}J_{SC}$, where A is the active area), respectively. In this case, as light intensity decreases, the J_{SC} becomes significantly lower than V_{OC}, and γ_s approaches 0 ($FF_S = FF_0$). Thus, the relationship below is established.[9,52−54]

$$\begin{aligned} FF = FF_{Sh} &= FF_S[1 - (v_{oc} + 0.7)FF_S/v_{oc}(\gamma_{Sh})] \\ &= FF_0[1 - (v_{oc} + 0.7)FF_0/v_{oc}(\gamma_{Sh})] \end{aligned} \tag{4}$$

Here, FF_{Sh} and γ_{Sh} refer to the shunt fill factor and the normalized shunt resistance (R_{Sh}/R_{ch}), respectively. As a result, the FF is significantly affected by γ_{sh} in indoor irradiation, and it is determined by R_{Sh}. As summarized in Table 1, the R_{Sh} of devices with the pristine ZnO layer and the GQD-doped ZnO layer were measured to be 874 and 2127 Ω cm^2, respectively. Furthermore, the R_{Sh} of devices with the pristine ZnO layer, which was measured at 1000 and 200 lux, exhibited 90,180 and 125,269 Ω cm^2, respectively, while those of devices with the GQD-doped ZnO layer exhibited the high R_{Sh} of 104,971 and 132,511 Ω cm^2. Hence, the introduction of GQDs induced high R_{Sh} in indoor irradiation, thereby showing high performance.[55]

The dark $J−V$ curve (Figure 5) showed saturated current and lower leakage current compared with the pristine ZnO layer in reverse bias, owing to the introduction of the GQD-doped ZnO layer. Furthermore, all semi-log plots of the dark $J−V$ curve and the indoor $J−V$ curve showed high current properties in forward bias when the GQD-doped ZnO layer was introduced (Figure 5,b). Additionally, the carrier dissociation probability can be analyzed through photocurrent density−effective voltage ($J_{ph}−V_{eff}$) measurement (Figure 5c). For the saturation photocurrent (J_{sat}) that was calculated based on the measurement of the photocurrent under illumination and the dark condition, the GQD-doped ZnO layer exhibited a higher value of 23.03 mA cm^{-2} compared with the pristine ZnO layer that had a value of 20.6 mA cm^{-2}. The carrier dissociation probability (P_{diss}) (Figure 5d) that was calculated based on the J_{ph}/J_{sat} value was approximately 98.2% for the GQD-doped ZnO layer and approximately 97.1% for the pristine ZnO layer near V_{eff} = 1 V. Accordingly, the introduction of GQDs resulted in a high carrier dissociation probability.[56−58] According to these results, the introduction of GQDs resulted in high photogenerated carriers, exhibiting low recombination properties due to high carrier dissociation properties. For indoor irradiation, it is highly important to enhance remarkable J_{SC} and FF, and these results indicate that the introduction of GQDs enables efficient utilization of photogenerated carriers in a limited light intensity.

3.5. Morphological and Crystalline Properties. The contact angle and surface energy properties are shown in Figure S6. The pristine ZnO layer film exhibited around 33.3° of water and 38.0° of diiodomethane (DIM) contact angles, and then, the surface energy was calculated to be approximately 60.23 mN m^{-1}. As incorporating GQDs, the film exhibited contact angles of around 40.3 and 27.9° in the order of water and DIM, respectively, and a surface energy of approximately 58.54 mN m^{-1}, which indicates forming a hydrophobic surface. Also, the calculated surface energy of the BHJ layer was 51.11 mN m^{-1}, exhibiting highly enlarged dispersion (D) properties and the lowest surface energy, which indicates hydrophobic surface properties. In general, the materials with lower surface energy segregate into the air and film interface, while those with higher surface energy segregate into the film and electrode interface.[59] In addition, the materials or interfaces with similar surface energy tend to form good interfacial contact with each other.[60] Consequently, the hydrophobic surface properties of the GQD-doped ZnO layer can form a good interface with the BHJ layer from the point of view of similarity of surface energy.[61,62]

In Figure 6, morphology characteristics of the pristine ZnO layer and GQD-doped ZnO layer were analyzed via field emission scanning electron microscopy (FE-SEM) and atomic force microscopy (AFM) measurement. The pristine ZnO layer exhibited large agglomerates (root mean square, R_q = 2.57 nm, in Figures 6a−c), which are consistent with large grains in Figure 6a. The GQD-doped ZnO layer showed a flat and uniform surface. There were some dispersed parts in dot shapes (only some of them were marked with yellow circles in Figure 6e,d) where GQDs are partially located. Even though a small part with dot shapes formed, the introduction of GQDs served a relatively flat and uniform surface with slightly lower roughness (R_q = 2.36 nm). Moreover, the BHJ layer film
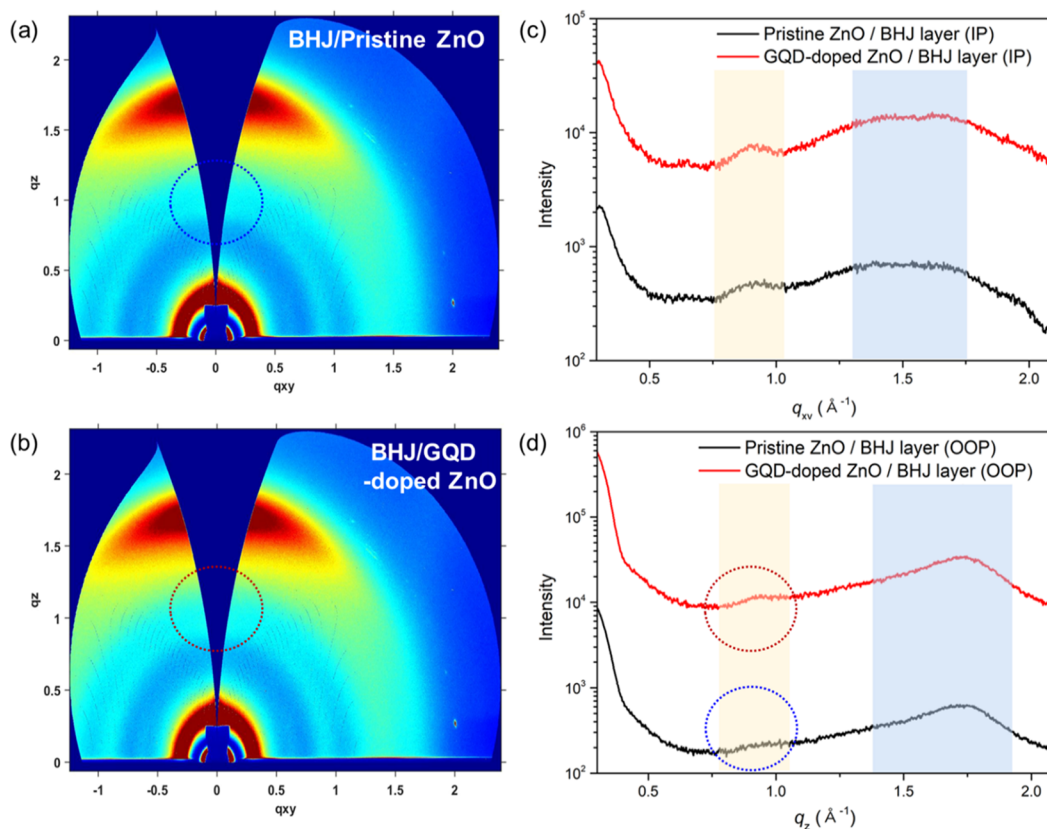
Figure 7. GIWAXS characteristics of BHJ layers coated on (a) pristine ZnO layer and (b) GQD-doped ZnO layer. Line-cut profile characteristics of BHJ layers coated on ZnO layers along with (c) in-plane direction and (d) out-of-plane direction.

coated on the GQD-doped ZnO layer exhibited a continuous and well-defined morphology compared with the one on the pristine ZnO layer (in Figures S7 and S8). With these results, our strategy of introducing GQDs not only enhanced optical properties from energy transfer but also helped in modifying surface properties, contributing to the enhancement of performances.

Furthermore, crystalline structures and line-cut profile characteristics of BHJ layers coated onto the pristine ZnO layer and GQD-doped ZnO layer were measured using grazing incidence wide-angle X-ray scattering (GIWAXS) and are shown in Figure 7 and Table S3. Both the BHJ layers coated on other ZnO layers exhibited clear face-on dominant molecular stacking with the (010) peak with $q_z = 1.75$ Å^{-1} in the out-of-plane direction.[63,64] In particular, the BHJ layers with the pristine ZnO layer and GQD-doped ZnO layer exhibited the (100) peaks at 0.31 and 0.30 Å^{-1} with lamellar stacking distances of 2.01 and 2.07 nm. However, in the GQD-doped ZnO layer, the (200) peak was noticeably increased at $q_z = 0.92$ Å^{-1} with a lamellar packing of 0.68 nm. In addition, in the out-of-plane direction, two films exhibited similar molecular stacking with strong intensity of the (010) peak with $\pi-\pi$ stacking distance around 0.35−0.36 nm. Furthermore, the calculated full width at half maximum (FWHM) values of the (010) peaks of the BHJ layer coated onto the pristine ZnO layer and GQD-doped ZnO layer were 0.404 and 0.351 Å^{-1}, and calculated crystalline coherence length (CCL) values through the Scherrer equation (CCL $= 2\pi K$/FWHM, $K =$ shape factor, 0.9) were 13.997 and 16.110 Å, respectively. These results of morphological and crystalline properties imply that the GQD-doped ZnO layer can form good interfacial

matching and more crystalline structure favorable for high performances.[65,66]

3.6. Carrier Recombination Properties. The flat and uniform morphology characteristics of the GQD-doped ZnO layer were helpful for the dissociation and transportation of photogenerated carriers. The dependences on light intensity of V_{OC} and J_{SC} are shown in Figure S9 for proving carrier recombination in all devices. Usually, V_{OC} has the following relationship with light intensity (I): $V_{OC} \propto kT/q\ln(I)$.[67,68] In ideal devices, the slope of kT/q approaches 1 when the devices have minimum trap-assisted carrier recombination. The device with the pristine ZnO layer exhibited a slope of 1.064 kT/q, while the device with the GQD-doped ZnO layer exhibited a slope of 1.048 kT/q. Furthermore, J_{SC} has the following power law relationship with I: $J_{SC} \propto I^\alpha$.[67,69] In this relationship, as the value of α approaches 1, it reflects suppressed bimolecular recombination. The device with the pristine ZnO layer exhibited an α of 0.970, while the device with the GQD-doped ZnO layer exhibited an α of 0.991. These relationships indicate that the GQDs not only control bimolecular recombination but also trap-assisted recombination.

Additionally, time-resolved photoluminescence (TRPL) decay and imaging measurement were performed for analyzing carrier lifetime (shown in Figure S10). The pristine ZnO and GQD-doped ZnO films were analyzed with a 375 nm single-mode pulsed diode laser. The calculated carrier lifetime of the pristine ZnO film was approximately 77 ns, while that of the GQD-doped ZnO film was 28 ns. The lifetime of the GQD-doped ZnO film was shorter, which indicates faster carrier transport before nongeminate recombination occurred.[70,71] With morphological benefits, the introduction of GQDs helped
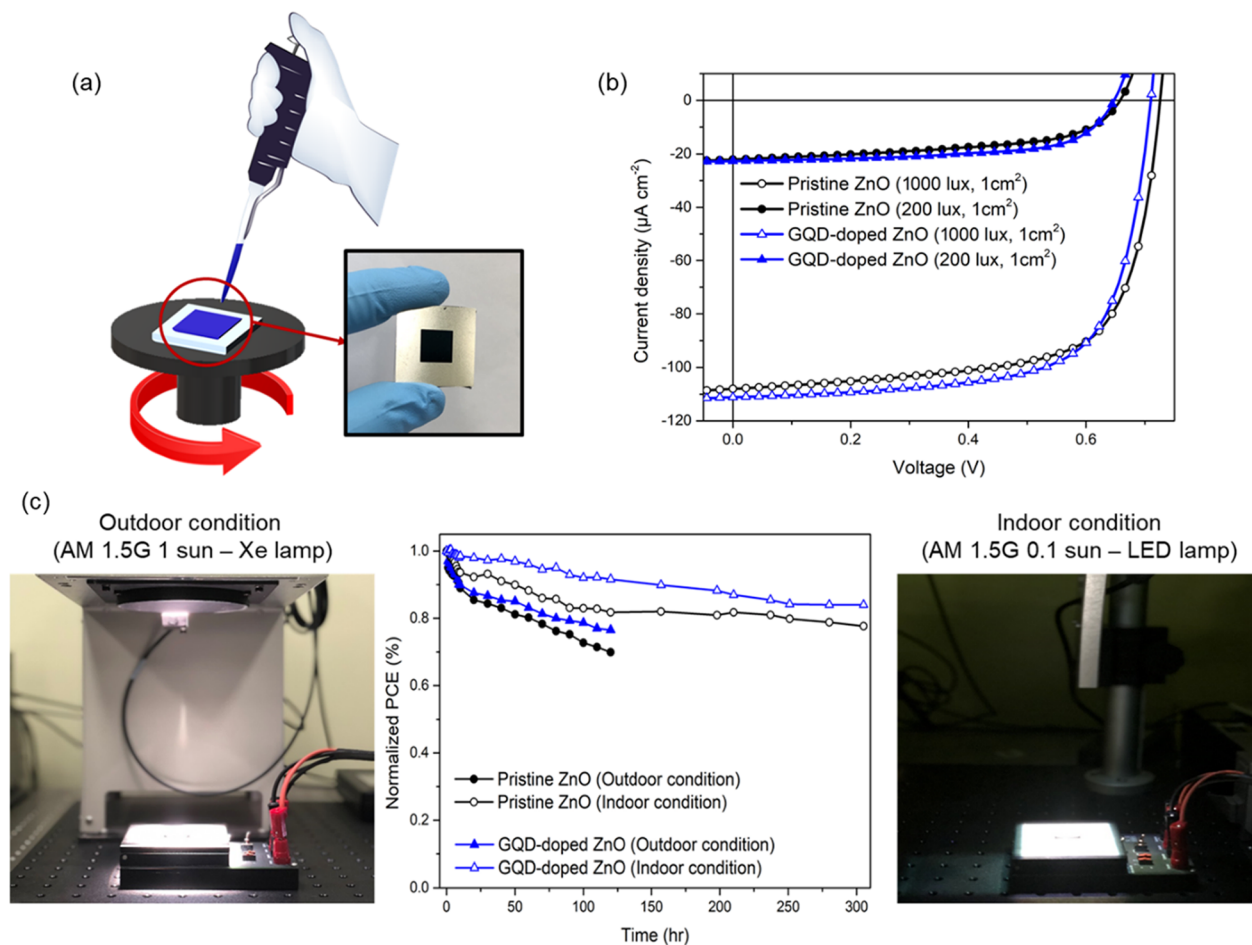
Figure 8. (a) Schematic image of a large-area device with an active area of 1.0 cm^2 via a spin-coating process. (b) Indoor $J-V$ characteristics of fabricated devices with the pristine ZnO layer and GQD-doped ZnO layer under 1000 and 200 lux of an LED lamp (5000 K). (c) Light-soaking stability characteristics in both outdoor conditions (AM 1.5G 1 sun irradiation of a xenon lamp) and indoor conditions (AM 1.5G 0.1 sun irradiation of an LED lamp) with images of the characterization environment.

Table 3. Photovoltaic Performances of Fabricated Large-Area OSCs (Active Area of 1.0 cm^2) under Different Light Intensities under 1 Sun and Indoor Irradiation[a]

ETLs	light source [lux]	P_{in} [μW cm^{-2}]	J_{SC} [μA cm^{-2}]	V_{OC} [V]	FF [%]	$P_{out, max}$ [μW cm^{-2}]	PCE$_{max}$[b] [%]
Pristine ZnO (1 cm^2)	1 sun	100 [mW cm^{-2}]	20.9 [mA cm^{-2}] (20.7 ± 0.21)	0.878 (0.868 ± 0.01)	58.0 (57.6 ± 0.39)	10.6 [mW cm^{-2}]	10.6
	200	62.8	22.1 (21.7 ± 0.43)	0.657 (0.637 ± 0.02)	50.6 (50.1 ± 0.51)	7.93	11.7
	1000	320.2	107.9 (107.4 ± 0.53)	0.725 (0.705 ± 0.02)	64.1 (63.8 ± 0.32)	53.27	15.7
GQD-doped ZnO (1 cm^2)	1 sun	100 [mW cm^{-2}]	21.9 [mA cm^{-2}] (21.7 ± 0.22)	0.858 (0.848 ± 0.01)	62.3 (62.0 ± 0.29)	11.7 [mW cm^{-2}]	11.7
	200	62.8	22.7 (22.4 ± 0.34)	0.647 (0.627 ± 0.02)	63.2 (62.9 ± 0.33)	9.27	14.8
	1000	320.2	111.1 (110.7 ± 0.41)	0.710 (0.700 ± 0.01)	69.5 (69.3 ± 0.24)	54.82	17.1

[a]Devices were fabricated with inverted structure (ITO/ETLs/BHJ layer/MoO$_3$/Ag, active area = 1.0 cm^2). [b]The maximum value was obtained from the best performance among 10 fabricated devices.

in efficient carrier dissociation, which indicates low leakage structure resulting in high R_{Sh} under both outdoor and indoor environments.

3.7. Application for Large-Area Device and Stability Properties. We fabricated a large-area device with an active area of 1.0 cm^2 via spin-coating. A schematic image of the fabrication process and an image of the device, indoor $J-V$ characteristics, and photovoltaic performances are shown in Figure 8 and Table 3. The introduction of GQDs enhanced the J_{SC} and FF under 1 sun, 1000 lux, and 200 lux irradiations. In

particular, the introduction of GQDs resulted in high FF in 200 lux irradiation, which are the results from the improved R_{Sh} (from 80,708 to 128,211 Ω cm^2).[55]

We also analyzed light-soaking stability characteristics in both outdoor and indoor conditions (shown in Figure 8c). The typical measurement environment of outdoor conditions and indoor conditions was determined with AM 1.5G 1 sun irradiation of a xenon lamp and 0.1 sun of a LED lamp. The device with the GQD-doped ZnO layer exhibited a reduction rate of 23.5% for outdoor conditions after 120 h and 16.0% for

indoor conditions after 300 h. In both outdoor and indoor conditions, the device introducing GQD-doped ZnO exhibited outstanding optical stability with reduction rates of less than 20% from initial states. These properties imply that the strategy of introducing the GQD-doped ZnO layer can guarantee effective power generation in both outdoor and indoor conditions.

Furthermore, the devices that were manufactured by introducing the GQD-doped ZnO layer were stored in a glovebox for 1200 h to evaluate the stability properties (shown in Figure S11). The evaluation results on stability properties showed that the PCE of devices was maintained at 94.2%, exhibiting remarkable stability properties, contrary to the PCE of the devices with the pristine ZnO layer at 71.2%. The reduction in the PCE of the device with the pristine ZnO layer occurred mainly owing to the reduction in FF, and the device with the GQD-doped ZnO layer exhibited excellent stability properties. These results are due to improved interfacial contact and morphological benefits from the introduction of GQDs resulting in high R_{Sh} favorable for efficient carrier dissociation.

4. CONCLUSIONS

This study introduced GQDs exhibiting unique optical properties as additional emitting materials under the strategy for universal utilization of OPVs in outdoor and indoor environments. GQDs enhanced the optical properties of OPVs by having strong emission properties through the lattice vibration and down-conversion properties. The manufactured devices showed remarkably enhanced J_{SC} and FF properties according to the measurement in the 1 sun and indoor irradiation environment. These results indicate that the GQD-doped ZnO layer showed stronger emission property improvement. This is because directional photon transfer occurred upon excitation of P(Cl-Cl)(BDD = 0.2). This increased photogenerated carriers and significantly improved J_{SC}. Moreover, the introduction of the GQD-doped ZnO layer induced high R_{Sh} due to good interfacial contact, resulting in a significant increase in FF as shown in the analysis of the Shockley−Queisser model. Furthermore, the introduction of GQDs improved R_{Sh}, and its formation of flat and uniform morphology significantly reduced not only bimolecular recombination but also trap-assisted carrier recombination. Consequently, the directional photon transfer that occurred owing to the introduction of GQDs exhibited efficient utilization of photons and enhanced effective photogenerated carrier properties, all showing a high performance in the 1 sun and indoor irradiation environments (14.0% under 1 sun and 19.6% under 1000 lux irradiation). Furthermore, a large-area device with GQDs exhibited a high performance of up to 17.1% in 1000 lux irradiation. Moreover, shunt resistance improved by the introduction of the GQD-doped ZnO layer contributed to the significantly improved stability of the manufactured devices. These results indicate that OPVs have potential for various industrial applications, including off-grid power supply and IoT sensors, in which OPVs can be used in both outdoor and indoor environments by presenting strategies that can show efficient photon utilization characteristics.

ASSOCIATED CONTENT

Ⓢⁱ Supporting Information

The Supporting Information is available free of charge at https://pubs.acs.org/doi/10.1021/acsami.0c09539.

> Experimental data of the $J–V$ curve, absolute irradiation and integrated power, IQE and reflectance, FF against light intensity, contact angle, FE-SEM, AFM measurement, molecular stacking distance properties, V_{OC} and J_{SC} dependence on light intensity, TRPL, and stability properties (PDF)

AUTHOR INFORMATION

Corresponding Author

Doo Kyung Moon − *Nano and Information Materials Lab. (NIMs Lab.), Department of Chemical Engineering, Konkuk University, Seoul 05029, Republic of Korea;* ⓞ orcid.org/0000-0001-9482-7508; Phone: +82-2-450-3498; Email: dkmoon@konkuk.ac.kr; Fax: +82-2-444-0765

Authors

Yong Woon Han − *Nano and Information Materials Lab. (NIMs Lab.), Department of Chemical Engineering, Konkuk University, Seoul 05029, Republic of Korea*

Chang Ho Jung − *Nano and Information Materials Lab. (NIMs Lab.), Department of Chemical Engineering, Konkuk University, Seoul 05029, Republic of Korea*

Hyoung Seok Lee − *Nano and Information Materials Lab. (NIMs Lab.), Department of Chemical Engineering, Konkuk University, Seoul 05029, Republic of Korea*

Sung Jae Jeon − *Nano and Information Materials Lab. (NIMs Lab.), Department of Chemical Engineering, Konkuk University, Seoul 05029, Republic of Korea*

Complete contact information is available at:
https://pubs.acs.org/10.1021/acsami.0c09539

Author Contributions

The manuscript was written through contributions of all authors. All authors have given approval to the final version of the manuscript.

Notes

The authors declare no competing financial interest.

REFERENCES

(1) Meng, X.; Zhang, L.; Xie, Y.; Hu, X.; Xing, Z.; Huang, Z.; Liu, C.; Tan, L.; Zhou, W.; Sun, Y.; Ma, W.; Chen, Y. A General Approach for Lab-to-Manufacturing Translation on Flexible Organic Solar Cells. *Adv. Mater.* **2019**, *31*, 1903649.

(2) Han, Y. W.; Song, H. J.; Jeon, S. J.; Lee, H. S.; Ko, E. J.; Song, C. E.; Sung, T. H.; Moon, D. K. Excellent Carrier Transport Materials Produced by Controlled Molecular Stacking and Their Application in Flexible Organic Electronic Devices. *J. Mater. Chem. A* **2019**, *7*, 14790−14805.

(3) Su, W.; Fan, Q.; Guo, X.; Wu, J.; Zhang, M.; Li, Y. Efficient As-Cast Semi-Transparent Organic Solar Cells with Efficiency over 9% and a High Average Visible Transmittance of 27.6%. *Phys. Chem. Chem. Phys.* **2019**, *21*, 10660−10666.

(4) Venkateswararao, A.; Ho, J. K. W.; So, S. K.; Liu, S. W.; Wong, K. T. Device Characteristics and Material Developments of Indoor Photovoltaic Devices. *Mater. Sci. Eng. R Rep.* **2020**, *139*, 100517.

(5) Cui, Y.; Yao, H.; Zhang, J.; Zhang, T.; Wang, Y.; Hong, L.; Xian, K.; Xu, B.; Zhang, S.; Peng, J.; Wei, Z.; Gao, F.; Hou, J. Over 16% Efficiency Organic Photovoltaic Cells Enabled by a Chlorinated Acceptor with Increased Open-Circuit Voltages. *Nat. Commun.* **2019**, *10*, 2515.

(6) Lin, Y.; Adilbekova, B.; Firdaus, Y.; Yengel, E.; Faber, H.; Sajjad, M.; Zheng, X.; Yarali, E.; Seitkhan, A.; Bakr, O. M.; El-Labban, A.; Schwingenschlögl, U.; Tung, V.; McCulloch, I.; Laquai, F.; Anthopoulos, T. D. 17% Efficient Organic Solar Cells Based on Liquid Exfoliated WS2 as a Replacement for PEDOT:PSS. *Adv. Mater.* **2019**, *31*, 1902965.

(7) Liu, L.; Kan, Y.; Gao, K.; Wang, J.; Zhao, M.; Chen, H.; Zhao, C.; Jiu, T.; Jen, A. K. Y.; Li, Y. Graphdiyne Derivative as Multifunctional Solid Additive in Binary Organic Solar Cells with 17.3% Efficiency and High Reproductivity. *Adv. Mater.* **2020**, *32*, 1907604.

(8) Han, Y. W.; Jeon, S. J.; Lee, H. S.; Park, H.; Kim, K. S.; Lee, H. W.; Moon, D. K. Evaporation-Free Nonfullerene Flexible Organic Solar Cell Modules Manufactured by An All-Solution Process. *Adv. Energy Mater.* **2019**, *9*, 1902065.

(9) Cui, Y.; Wang, Y.; Bergqvist, J.; Yao, H.; Xu, Y.; Gao, B.; Yang, C.; Zhang, S.; Inganäs, O.; Gao, F.; Hou, J. Wide-Gap Non-Fullerene Acceptor Enabling High-Performance Organic Photovoltaic Cells for Indoor Applications. *Nat. Energy* **2019**, *4*, 768−775.

(10) Reynaud, C. A.; Clerc, R.; Lechêne, P. B.; Hébert, M.; Cazier, A.; Arias, A. C. Evaluation of Indoor Photovoltaic Power Production under Directional and Diffuse Lighting Conditions. *Sol. Energy Mater. Sol. Cells* **2019**, *200*, 110010.

(11) Aoki, Y. Photovoltaic Performance of Organic Photovoltaics for Indoor Energy Harvester. *Org. Electron.* **2017**, *48*, 194−197.

(12) Cutting, C. L.; Bag, M.; Venkataraman, D. Indoor Light Recycling: A New Home for Organic Photovoltaics. *J. Mater. Chem. C* **2016**, *4*, 10367−10370.

(13) Yan, T.; Song, W.; Huang, J.; Peng, R.; Huang, L.; Ge, Z. 16.67% Rigid and 14.06% Flexible Organic Solar Cells Enabled by Ternary Heterojunction Strategy. *Adv. Mater.* **2019**, *31*, 1902210.

(14) Kan, B.; Yi, Y. Q. Q.; Wan, X.; Feng, H.; Ke, X.; Wang, Y.; Li, C.; Chen, Y. Ternary Organic Solar Cells With 12.8% Efficiency Using Two Nonfullerene Acceptors With Complementary Absorptions. *Adv. Energy Mater.* **2018**, *8*, 1800424.

(15) Teng, N. W.; Yang, S. S.; Chen, F. C. Plasmonic-Enhanced Organic Photovoltaic Devices for Low-Power Light Applications. *IEEE J. Photovoltaics* **2018**, *8*, 752−756.

(16) Ho, J. K. W.; Yin, H.; So, S. K. From 33% to 57%-An Elevated Potential of Efficiency Limit for Indoor Photovoltaics. *J. Mater. Chem. A* **2020**, *8*, 1717−1723.

(17) Yu, X.; Yu, X.; Hu, Z.; Zhang, J.; Zhao, G.; Zhao, Y. Effect of Sol-Gel Derived ZnO Annealing Rate on Light-Trapping in Inverted Polymer Solar Cells. *Mater. Lett.* **2013**, *108*, 50−53.

(18) Nam, M.; Baek, S.; Ko, D. H. Unraveling Optimal Interfacial Conditions for Highly Efficient and Reproducible Organic Photovoltaics under Low Light Levels. *Appl. Surf. Sci.* **2020**, *526*, 146632.

(19) Torimtubun, A. A. A.; Sánchez, J. G.; Pallarès, J.; Marsal, L. F. A Cathode Interface Engineering Approach for the Comprehensive Study of Indoor Performance Enhancement in Organic Photovoltaics. *Sustain. Energy Fuels* **2020**, *4*, 3378−3387.

(20) Arai, R.; Furukawa, S.; Hidaka, Y.; Komiyama, H.; Yasuda, T. High-Performance Organic Energy-Harvesting Devices and Modules for Self-Sustainable Power Generation under Ambient Indoor Lighting Environments. *ACS Appl. Mater. Interfaces* **2019**, *11*, 9259−9264.

(21) Gilot, J.; Barbu, I.; Wienk, M. M.; Janssen, R. A. J. The Use of ZnO as Optical Spacer in Polymer Solar Cells: Theoretical and Experimental Study. *Appl. Phys. Lett.* **2007**, *91*, 113520.

(22) Steim, R.; Kogler, F. R.; Brabec, C. J. Interface Materials for Organic Solar Cells. *J. Mater. Chem.* **2010**, *20*, 2499−2512.

(23) Mainville, M.; Leclerc, M. Recent Progress on Indoor Organic Photovoltaics: From Molecular Design to Production Scale. *ACS Energy Lett.* **2020**, *5*, 1186−1197.

(24) Trost, S.; Zilberberg, K.; Behrendt, A.; Polywka, A.; Görrn, P.; Reckers, P.; Maibach, J.; Mayer, T.; Riedl, T. Overcoming the "Light-Soaking" Issue in Inverted Organic Solar Cells by the Use of Al:ZnO Electron Extraction Layers. *Adv. Energy Mater.* **2013**, *3*, 1437−1444.

(25) Cheng, P.; Zhan, X. Stability of Organic Solar Cells: Challenges and Strategies. *Chem. Soc. Rev.* **2016**, *45*, 2544−2582.

(26) Li, X.; Liu, X.; Zhang, W.; Wang, H.-Q.; Fang, J. Fullerene-Free Organic Solar Cells with Efficiency Over 12% Based on EDTA-ZnO Hybrid Cathode Interlayer. *Chem. Mater.* **2017**, *29*, 4176−4180.

(27) Han, Y. W.; Lee, E. J.; Joo, J.; Park, J.; Sung, T. H.; Moon, D. K. Photon Energy Transfer by Quantum Dots in Organic-Inorganic Hybrid Solar Cells through FRET. *J. Mater. Chem. A* **2016**, *4*, 10444−10453.

(28) Han, Y. W.; Jeon, S. J.; Choi, J. Y.; Kim, J. H.; Moon, D. K. Highly Efficient Ternary Solar Cells of 10.2% with Core/Shell Quantum Dots via FRET Effect. *Sol. RRL* **2018**, *2*, 1800077.

(29) Lee, C. Y.; Hupp, J. T. Dye Sensitized Solar Cells: TiO2 Sensitization with a Bodipy-Porphyrin Antenna System. *Langmuir* **2010**, *26*, 3760−3765.

(30) Liu, Q.; Sun, J.; Gao, K.; Chen, N.; Sun, X.; Ti, D.; Bai, C.; Cui, R.; Qu, L. Graphene Quantum Dots for Energy Storage and Conversion: From Fabrication to Applications. *Mater. Chem. Front.* **2020**, *4*, 421−436.

(31) Shen, J.; Zhu, Y.; Yang, X.; Li, C. Graphene Quantum Dots: Emergent Nanolights for Bioimaging, Sensors, Catalysis and Photovoltaic Devices. *Chem. Commun* **2012**, *48*, 3686−3699.

(32) Kim, J. K.; Park, M. J.; Kim, S. J.; Wang, D. H.; Cho, S. P.; Bae, S.; Park, J. H.; Hong, B. H. Balancing Light Absorptivity and Carrier Conductivity of Graphene Quantum Dots for High-Efficiency Bulk Heterojunction Solar Cells. *ACS Nano* **2013**, *7*, 7207−7212.

(33) Moon, B. J.; Jang, D.; Yi, Y.; Lee, H.; Kim, S. J.; Oh, Y.; Lee, S. H.; Park, M.; Lee, S.; Bae, S. Multi-Functional Nitrogen Self-Doped Graphene Quantum Dots for Boosting the Photovoltaic Performance of BHJ Solar Cells. *Nano Energy* **2017**, *34*, 36−46.

(34) Novak, T. G.; Kim, J.; Song, S. H.; Jun, G. H.; Kim, H.; Jeong, M. S.; Jeon, S. Fast P3HT Exciton Dissociation and Absorption Enhancement of Organic Solar Cells by PEG-Functionalized Graphene Quantum Dots. *Small* **2016**, *12*, 994−999.

(35) Jeon, S. J.; Han, Y. W.; Moon, D. K. 13.9%-Efficiency and Eco-Friendly Nonfullerene Polymer Solar Cells Obtained by Balancing Molecular Weight and Solubility in Chlorinated Thiophene-Based Polymer Backbones. *Small* **2019**, *15*, 1902598.

(36) Li, H.; Wang, J.; Liu, H.; Yang, C.; Xu, H.; Li, X.; Cui, H. Sol-Gel Preparation of Transparent Zinc Oxide Films with Highly Preferential Crystal Orientation. *Vacuum* **2004**, *77*, 57−62.

(37) Li, L.; Wu, G.; Yang, G.; Peng, J.; Zhao, J.; Zhu, J. J. Focusing on Luminescent Graphene Quantum Dots: Current Status and Future Perspectives. *Nanoscale* **2013**, *5*, 4015−4039.

(38) Leung, Y. H.; Chen, X. Y.; Ng, A. M. C.; Guo, M. Y.; Liu, F. Z.; Djurišić, A. B.; Chan, W. K.; Shi, X. Q.; Van Hove, M. A. Green Emission in ZnO Nanostructures-Examination of the Roles of Oxygen and Zinc Vacancies. *Appl. Surf. Sci.* **2013**, *271*, 202−209.

(39) Bai, S.; Jin, Y.; Liang, X.; Ye, Z.; Wu, Z.; Sun, B.; Ma, Z.; Tang, Z.; Wang, J.; Würfel, U.; Gao, F.; Zhang, F. Ethanedithiol Treatment of Solution-Processed ZnO Thin Films: Controlling the Intragap States of Electron Transporting Interlayers for Efficient and Stable Inverted Organic Photovoltaics. *Adv. Energy Mater.* **2015**, *5*, 1401606.

(40) Shin, S. C.; Koh, C. W.; Vincent, P.; Goo, J. S.; Bae, J. H.; Lee, J. J.; Shin, C.; Kim, H.; Woo, H. Y.; Shim, J. W. Ultra-Thick Semi-Crystalline Photoactive Donor Polymer for Efficient Indoor Organic Photovoltaics. *Nano Energy* **2019**, *58*, 466−475.

(41) Cheng, H.-W.; Zhang, H.; Lin, Y.-C.; She, N.-Z.; Wang, R.; Chen, C.-H.; Yuan, J.; Tsao, C.-S.; Yabushita, A.; Zou, Y.; Gao, F.; Cheng, P.; Wei, K.-H.; Yang, Y. Realizing Efficient Charge/Energy Transfer and Charge Extraction in Fullerene-Free Organic Photovoltaics via a Versatile Third Component. *Nano Lett.* **2019**, *19*, 5053−5061.

(42) Yang, W.; Ye, Z.; Liang, T.; Ye, J.; Chen, H. Facilitate Charge Transfer at Donor/Acceptor Interface in Bulk Heterojunction

Organic Photovoltaics by Two-Dimensional Nanoflakes. *Sol. Energy Mater. Sol. Cells* **2019**, *190*, 75−82.

(43) Ma, X.; Luo, M.; Gao, W.; Yuan, J.; An, Q.; Zhang, M.; Hu, Z.; Gao, J.; Wang, J.; Zou, Y.; Yang, C.; Zhang, F. Achieving 14.11% Efficiency of Ternary Polymer Solar Cells by Simultaneously Optimizing Photon Harvesting and Exciton Distribution. *J. Mater. Chem. A* **2019**, *7*, 7843−7851.

(44) Atxabal, A.; Braun, S.; Arnold, T.; Sun, X.; Parui, S.; Liu, X.; Gozalvez, C.; Llopis, R.; Mateo-Alonso, A.; Casanova, F.; Ortmann, F.; Fahlman, M.; Hueso, L. E. Energy Level Alignment at Metal/Solution-Processed Organic Semiconductor Interfaces. *Adv. Mater.* **2017**, *29*, 1606901.

(45) Wang, H.; Gomez, E. D.; Guan, Z.; Jaye, C.; Toney, M. F.; Fischer, D. A.; Kahn, A.; Loo, Y.-L. Tuning Contact Recombination and Open-Circuit Voltage in Polymer Solar Cells via Self-Assembled Monolayer Adsorption at the Organic-Metal Oxide Interface. *J. Phys. Chem. C* **2013**, *117*, 20474−20484.

(46) Sengupta, J.; Sahoo, R. K.; Bardhan, K. K.; Mukherjee, C. D. Influence of Annealing Temperature on the Structural, Topographical and Optical Properties of Sol-Gel Derived ZnO Thin Films. *Mater. Lett.* **2011**, *65*, 2572−2574.

(47) Li, M.; Ni, W.; Kan, B.; Wan, X.; Zhang, L.; Zhang, Q.; Long, G.; Zuo, Y.; Chen, Y. Graphene Quantum Dots as the Hole Transport Layer Material for High-Performance Organic Solar Cells. *Phys. Chem. Chem. Phys.* **2013**, *15*, 18973−18978.

(48) Vidyasagar, R.; Camargo, B.; Romanyuk, K.; Kholkin, A. L. Surface Potential Distribution of Multilayer Graphene Using Kelvin Probe and Electric-Field Force Microscopies. *Ferroelectrics* **2017**, *508*, 115−123.

(49) Tang, Y.; Sun, H.; Wu, Z.; Zhang, Y.; Zhang, G.; Su, M.; Zhou, X.; Wu, X.; Sun, W.; Zhang, X.; Liu, B.; Chen, W.; Liao, Q.; Woo, H. Y.; Guo, X. A New Wide Bandgap Donor Polymer for Efficient Nonfullerene Organic Solar Cells with a Large Open-Circuit Voltage. *Adv. Sci.* **2019**, *6*, 1901773.

(50) Park, S. H.; Roy, A.; Beaupré, S.; Cho, S.; Coates, N.; Moon, J. S.; Moses, D.; Leclerc, M.; Lee, K.; Heeger, A. J. Bulk Heterojunction Solar Cells with Internal Quantum Efficiency Approaching 100%. *Nat. Photonics* **2009**, *3*, 297−302.

(51) Würfel, U.; Neher, D.; Spies, A.; Albrecht, S. Impact of Charge Transport on Current-Voltage Characteristics and Power-Conversion Efficiency of Organic Solar Cells. *Nat. Commun.* **2015**, *6*, 6951.

(52) Qi, B.; Wang, J. Fill Factor in Organic Solar Cells. *Phys. Chem. Chem. Phys.* **2013**, *15*, 8972−8982.

(53) Janssen, R. A. J.; Nelson, J. Factors Limiting Device Efficiency in Organic Photovoltaics. *Adv. Mater.* **2013**, *25*, 1847−1858.

(54) Trukhanov, V. A.; Bruevich, V. V.; Paraschuk, D. Y. Fill Factor in Organic Solar Cells Can Exceed the Shockley-Queisser Limit. *Sci. Rep* **2015**, *5*, 11478.

(55) Park, S. Y.; Li, Y.; Kim, J.; Lee, T. H.; Walker, B.; Woo, H. Y.; Kim, J. Y. Alkoxybenzothiadiazole-Based Fullerene and Nonfullerene Polymer Solar Cells with High Shunt Resistance for Indoor Photovoltaic Applications. *ACS Appl. Mater. Interfaces* **2018**, *10*, 3885−3894.

(56) He, Z.; Zhong, C.; Huang, X.; Wong, W. Y.; Wu, H.; Chen, L.; Su, S.; Cao, Y. Simultaneous Enhancement of Open-Circuit Voltage, Short-Circuit Current Density, and Fill Factor in Polymer Solar Cells. *Adv. Mater.* **2011**, *23*, 4636−4643.

(57) Mullenbach, T. K.; Holmes, R. J. Relating Photocurrent, Photovoltage, and Charge Carrier Density to the Recombination Rate in Organic Photovoltaic Cells. *Appl. Phys. Lett.* **2015**, *107*, 123303.

(58) Chen, M.; Zhang, Z.; Li, W.; Cai, J.; Yu, J.; Spooner, E. L. K.; Kilbride, R. C.; Li, D.; Du, B.; Gurney, R. S.; Liu, D.; Tang, W.; Lidzey, D. G.; Wang, T. Regulating the Morphology of Fluorinated Non-Fullerene Acceptor and Polymer Donor via Binary Solvent Mixture for High Efficiency Polymer Solar Cells. *Sci. China Chem.* **2019**, *62*, 1221−1229.

(59) Honda, S.; Ohkita, H.; Benten, H.; Ito, S. Selective Dye Loading at the Heterojunction in Polymer/Fullerene Solar Cells. *Adv. Energy Mater.* **2011**, *1*, 588−598.

(60) Lee, S.; Park, K. H.; Lee, J. H.; Back, H.; Sung, M. J.; Lee, J.; Kim, J.; Kim, H.; Kim, Y. H.; Kwon, S. K.; Lee, K. Achieving Thickness-Insensitive Morphology of the Photoactive Layer for Printable Organic Photovoltaic Cells via Side Chain Engineering in Nonfullerene Acceptors. *Adv. Energy Mater.* **2019**, *9*, 1900044.

(61) Lee, E. J.; Heo, S. W.; Han, Y. W.; Moon, D. K. An Organic-Inorganic Hybrid Interlayer for Improved Electron Extraction in Inverted Polymer Solar Cells. *J. Mater. Chem. C* **2016**, *4*, 2463−2469.

(62) Zheng, Z.; Zhang, S.; Wang, J.; Zhang, J.; Zhang, D.; Zhang, Y.; Wei, Z.; Tang, Z.; Hou, J.; Zhou, H. Exquisite Modulation of ZnO Nanoparticle Electron Transporting Layer for High-Performance Fullerene-Free Organic Solar Cell with Inverted Structure. *J. Mater. Chem. A* **2019**, *7*, 3570−3576.

(63) Zhou, D.; Xiong, S.; Chen, L.; Cheng, X.; Xu, H.; Zhou, Y.; Liu, F.; Chen, Y. A Green Route to a Novel Hyperbranched Electrolyte Interlayer for Nonfullerene Polymer Solar Cells with over 11% Efficiency. *Chem. Commun.* **2018**, *54*, 563−566.

(64) Jeon, S. J.; Yu, J. E.; Han, Y. W.; Suh, I. S.; Moon, D. K. Structural Optimization in the Same Polymer Backbones for Efficient Polymer Solar Cells: Relationship between Steric Hindrance and Molecular Weight. *J. Ind. Eng. Chem.* **2019**, *71*, 137−149.

(65) Lin, Y.; Zhao, F.; Wu, Y.; Chen, K.; Xia, Y.; Li, G.; Prasad, S. K. K.; Zhu, J.; Huo, L.; Bin, H.; Zhang, Z. G.; Guo, X.; Zhang, M.; Sun, Y.; Gao, F.; Wei, Z.; Ma, W.; Wang, C.; Hodgkiss, J.; Bo, Z.; Inganäs, O.; Li, Y.; Zhan, X. Mapping Polymer Donors toward High-Efficiency Fullerene Free Organic Solar Cells. *Adv. Mater.* **2017**, *29*, 1604155.

(66) Gao, K.; Jo, S. B.; Shi, X.; Nian, L.; Zhang, M.; Kan, Y.; Lin, F.; Kan, B.; Xu, B.; Rong, Q.; Shui, L.; Liu, F.; Peng, X.; Zhou, G.; Cao, Y.; Jen, A. K. Y. Over 12% Efficiency Nonfullerene All-Small-Molecule Organic Solar Cells with Sequentially Evolved Multilength Scale Morphologies. *Adv. Mater.* **2019**, *31*, 1807842.

(67) Kyaw, A. K. K.; Wang, D. H.; Gupta, V.; Leong, W. L.; Ke, L.; Bazan, G. C.; Heeger, A. J. Intensity Dependence of Current-Voltage Characteristics and Recombination in High-Efficiency Solution-Processed Small-Molecule Solar Cells. *ACS Nano* **2013**, *7*, 4569−4577.

(68) Elumalai, N. K.; Uddin, A. Open Circuit Voltage of Organic Solar Cells: An in-Depth Review. *Energy Environ. Sci.* **2016**, *9*, 391−410.

(69) Proctor, C. M.; Nguyen, T. Q. Effect of Leakage Current and Shunt Resistance on the Light Intensity Dependence of Organic Solar Cells. *Appl. Phys. Lett.* **2015**, *106*, No. 083301.

(70) Dong, S.; Liu, Y.; Hong, Z.; Yao, E.; Sun, P.; Meng, L.; Lin, Y.; Huang, J.; Li, G.; Yang, Y. Unraveling the High Open Circuit Voltage and High Performance of Integrated Perovskite/Organic Bulk-Heterojunction Solar Cells. *Nano Lett.* **2017**, *17*, 5140−5147.

(71) Cheng, P.; Li, G.; Zhan, X.; Yang, Y. Next-Generation Organic Photovoltaics Based on Non-Fullerene Acceptors. *Nat. Photonics* **2018**, *12*, 131−142.